



## Rapid synthesis of free-standing MoO<sub>3</sub>/Graphene films by the microwave hydrothermal method as cathode for bendable lithium batteries

Lukman Noerochim<sup>a,b,\*</sup>, Jia-Zhao Wang<sup>a,\*\*</sup>, David Wexler<sup>c</sup>, Zhong Chao<sup>a</sup>, Hua-Kun Liu<sup>a</sup>

<sup>a</sup> Institute for Superconducting and Electronic Materials, ARC Center of Excellence for Electromaterials Science, University of Wollongong, New South Wales 2500, Australia

<sup>b</sup> Department of Materials and Metallurgy, Sepuluh Nopember Institute of Technology, Surabaya 60111, Indonesia

<sup>c</sup> School of Mechanical, Materials and Mechatronic Engineering University of Wollongong, New South Wales 2522, Australia

### HIGHLIGHTS

- ▶ A new method to synthesize high quality of MoO<sub>3</sub> nanobelts from commercial bulk.
- ▶ Ultra-fast microwave hydrothermal method for fabrication MoO<sub>3</sub>/graphene films.
- ▶ MoO<sub>3</sub>/graphene hybrid materials demonstrate good cycling stability as cathode.

### ARTICLE INFO

#### Article history:

Received 22 September 2012

Received in revised form

26 November 2012

Accepted 28 November 2012

Available online 2 December 2012

#### Keywords:

Microwave

Hydrothermal

Free-standing film

MoO<sub>3</sub> nanobelt

Graphene

Cathode

### ABSTRACT

Highly flexible, binder-free, MoO<sub>3</sub> nanobelt/graphene film electrode is prepared by a two-step microwave hydrothermal method. Graphene is first prepared by an ultra-fast microwave hydrothermal method and then mixed with MoO<sub>3</sub> solution to synthesize the MoO<sub>3</sub> nanobelt/graphene composite, which exhibits the combination of stacked graphene sheets and uniform MoO<sub>3</sub> nanobelts with widths of 200–500 nm and lengths of 5–10 μm. The charge–discharge measurements show that the as-synthesized MoO<sub>3</sub>/graphene hybrid materials demonstrate excellent rate capability, large capacity, and good cycling stability compared to the pure MoO<sub>3</sub> film. An initial discharge capacity of 291 mAh g<sup>−1</sup> can be obtained at 100 mA g<sup>−1</sup>, with a capacity of 172 mAh g<sup>−1</sup> retained after 100 cycles. The results show that the MoO<sub>3</sub>/graphene designed in this study can be used as a free-standing cathode material in rechargeable bendable Lithium batteries.

© 2012 Elsevier B.V. All rights reserved.

### 1. Introduction

The invention of rechargeable lithium ion batteries has actively changed the functionality of the modern life style [1], with such batteries attracting great interest as a promising energy source due to their advantages over traditional rechargeable systems, such as environmental friendliness, large energy density, and high output voltage. Many efforts have been made to meet the requirements for their application in electric vehicles and electronic devices [2]. Recently, there has been a strong interest in and high demand for ultra-thin, flexible, safe energy storage devices to meet the various

design and power needs of modern electronic devices [3,4]. To build such fully flexible and robust electrochemical devices, electrodes with specific electrochemical and mechanical properties need to be explored to fulfil these requirements. Traditional Li-storage material electrodes suffer from serious cracking and poor physical properties when they are frequently bent or loaded by impact bending, which is mainly due to weak bonding between the materials and the current collector. A thin free-standing electrode film with complete mechanical flexibility during operation could solve these problems. Nanostructured electrode materials, particularly one-dimensional (1D) nanowires/nanorods/nanobelts [5–8], are considered to be the most promising avenue towards fabricating free-standing electrodes. The 1D nanowire, nanorod, or nanobelt morphology not only has a large electrode–electrolyte contact area and facile strain relaxation, but also efficient 1D electron transport pathways [5,6].

So far as free-standing cathode materials are concerned, there have been very few reports in the literature [9–11]. Therefore, it is still

\* Corresponding author. Institute for Superconducting and Electronic Materials, ARC Center of Excellence for Electromaterials Science, University of Wollongong, NSW 2500, Australia. Tel.: +61 2 42981494; fax: +61 2 4221 5731.

\*\* Corresponding author. Tel.: +61 2 4298 1478; fax: +61 2 4221 5731.

E-mail addresses: [ln865@uow.edu.au](mailto:ln865@uow.edu.au) (L. Noerochim), [jiazhao@uow.edu.au](mailto:jiazhao@uow.edu.au) (J.-Z. Wang).

a great challenge to explore an appropriate free-standing cathode material with high electrochemical performance for commercial application in bendable and wearable batteries. Among the known cathode materials for Li battery applications, molybdenum trioxide ( $\text{MoO}_3$ ) is one of the most important energy storage candidates, with high discharge capacity around  $300 \text{ mAh g}^{-1}$  [12–16].  $\text{MoO}_3$  is also a promising material in gas sensors [17] and catalysts for selective partial oxidation in modern industry [18,19].  $\text{MoO}_3$  has three basic polymorphs, i.e., orthorhombic  $\text{MoO}_3$ , monoclinic  $\text{MoO}_3$ , and hexagonal  $\text{MoO}_3$ . As cathode for the Li battery, orthorhombic  $\text{MoO}_3$  has been selected as a strong candidate due to its thermodynamically stable phase [14,20]. The orthorhombic  $\text{MoO}_3$  phase possesses a unique layered structure: each layer is composed of two sublayers, which are formed by corner-sharing  $[\text{MoO}_6]$  octahedra along the [001] and [100] directions, and the two sublayers are stacked together by sharing the edges of the octahedra along the [001] direction. The stacking of these layers along the [010] direction by the van der Waals interaction leads to the formation of  $\text{MoO}_3$  with a two-dimensional structure, which allows guest atoms and ions (such as  $\text{Li}^+$ ) to be introduced between the layers through intercalation [21]. In practical use for the Li battery,  $\text{MoO}_3$  has poor ionic and electronic conductivity [22]. To improve the conductivity of  $\text{MoO}_3$ , carbon nanotubes [11,23], graphene [24], or conducting polymer [25,26] could be the best choices of conductive fillers. Very recently, it was suggested that graphene, a new two-dimensional nanomaterial composed of  $\text{sp}^2$ -hybridized carbon, could be employed as an excellent candidate for the preparation of metal oxide–graphene nanocomposites due to its high conductivity, large surface area, flexibility, and chemical stability [27]. Metal oxide–graphene nanocomposites that have been prepared with different morphologies for specific applications include nanoparticle–graphene hybrids such as  $\text{Fe}_3\text{O}_4$ –graphene [28–30],  $\text{NiO}$ –graphene [31,32],  $\text{SnO}_2$ –graphene [33–35] and  $\text{LiFePO}_4$ –graphene [36,37].

There are several reports on the hydrothermal synthesis of  $\text{MoO}_3$  nanostructures to produce materials with high purity, homogeneity, good crystallinity, and unique properties [20,38–40]. Microwave irradiation can be used as an alternative heat source for the hydrothermal process [41,42]. It leads to a rapid heating to attain the desired temperature in a short time and increases the reaction kinetics compared to the conventional hydrothermal method. In a microwave-assisted hydrothermal reaction, the heating rate is extremely rapid, due to the dielectric property of the medium or solvent [41,42]. Recently, Phuruangrat [43] reported  $\text{MoO}_3$  nanowires 50 nm in diameter and 10–12  $\mu\text{m}$  in length that were synthesized by the microwave assisted hydrothermal method with cetyl trimethylammonium bromide (CTAB) as the surfactant-template.

Here, a new method to synthesize high quality  $\text{MoO}_3$  nanobelts from commercial bulk  $\text{MoO}_3$  without a surfactant-template and combine them with graphene via a two-step microwave hydrothermal method for fabrication of highly flexible free-standing  $\text{MoO}_3$ /graphene films is presented. The free-standing  $\text{MoO}_3$  nanobelt/graphene films prepared by the above method followed by the vacuum filtration technique were investigated as a cathode material for bendable Lithium batteries and compared with  $\text{MoO}_3$  nanobelt films prepared by a similar method but with no graphene.

## 2. Experimental

### 2.1. Preparation of $\text{MoO}_3$ nanobelt/graphene composite

The  $\text{MoO}_3$  nanobelt/graphene composite was synthesized by a two-step microwave hydrothermal method. Graphene oxide (GO) was prepared from natural graphite powder (Fluka) by a modified Hummers' method with additional  $\text{KMnO}_4$  [44]. In a typical

synthesis, 20 mg of GO was dispersed in 100 mL deionized water and sonicated for 30 min to yield graphene oxide nanosheets. After sonication, 100 mg NaOH (Sigma–Aldrich) and  $\text{H}_4\text{N}_2 \cdot \text{H}_2\text{O}$  (0.56 mL, Sigma–Aldrich) were added to the solution, followed by stirring for 10 min. After stirring, the mixture was transferred into a Teflon-lined microwave reactor (MicroSYNTH microwave system, Milestone), with the temperature controlled at  $120^\circ\text{C}$  for 15 min. After cooling down to room temperature, the graphene product was filtered and washed with deionized water. In a typical synthesis, 0.143 g of  $\text{MoO}_3$  powder (98%, Sigma–Aldrich) and 20 ml deionized water were mixed under vigorous magnetic stirring, and then 5 ml 30%  $\text{H}_2\text{O}_2$  (Sigma–Aldrich) was added to this mixed solution and kept continuously stirred on a hot plate with the temperature set to  $80^\circ\text{C}$  for 20 min until a transparent yellow solution was obtained. Then, the graphene product was gently mixed with the  $\text{MoO}_3$  solution for 10 min to yield a brown homogeneous suspension. The reaction solution was transferred to a 100 mL Teflon-lined autoclave and kept in a microwave oven (MicroSYNTH microwave system, Milestone) at  $180^\circ\text{C}$  for 30 min. The power, time, and temperature of the reaction system were controlled by a Lab-terminal 800 Controller. After naturally cooling to room temperature, the product was washed several times with distilled water.

### 2.2. Preparation of free-standing $\text{MoO}_3$ /graphene film

To make a uniform film, a modified vacuum filtration technique was adopted [45], where a 300 ml filter funnel (Glasco) was used. In a typical procedure,  $2 \text{ mg ml}^{-1}$  of  $\text{MoO}_3$ /graphene material was dispersed into 50 ml of distilled water. Then, the as-prepared suspension was poured into the funnel and filtered through a porous polyvinylidene fluoride (PVDF) membrane (Millipore,  $0.22 \mu\text{m}$  pore size, 47 mm in diameter) by positive pressure from a vacuum pump. Since the solvent passed through the pores of the membrane, the  $\text{MoO}_3$ /graphene material was trapped on the membrane surface, forming a mat. The resultant mat, together with the PVDF membrane, was then dried in an oven for 2 h, and the mat could finally be peeled off from the membrane as a free-standing  $\text{MoO}_3$ /graphene film. The mat could be directly used as electrode after drying at  $100^\circ\text{C}$  in a vacuum oven overnight.

### 2.3. Structure and morphology analysis

X-ray diffraction (XRD) data for phase analysis was obtained using a GBC MMA generator and diffractometer with  $\text{Cu K}\alpha$  radiation. Raman spectroscopy was conducted using a JOBIN YVON HR800 Confocal Raman system with 632.8 nm diode laser excitation on a 300 lines  $\text{mm}^{-1}$  grating at room temperature. This was performed in order to confirm the presence of graphene in the nanobelt products and to further investigate the  $\text{MoO}_3$ , and  $\text{MoO}_3$ /graphene films produced. The amount of graphene in the sample was estimated by thermogravimetric analysis (TGA) using a TGA/DSC 1 Star<sup>c</sup> System. The morphologies of the films were investigated by field emission scanning electron microscopy using a JEOL JSM-7500FA cold emission instrument. Transmission electron microscopy (TEM) and high resolution TEM was performed using JEOL 2011, 200 kV instrument. Samples for TEM were dispersed on Quantifoil holey carbon supports with analysis performed on regions over the holes.

### 2.4. Electrochemical measurements

To test the electrochemical performance of the  $\text{MoO}_3$ /graphene film as cathode, square model electrodes were cut off from the obtained free-standing film and then dried at  $100^\circ\text{C}$  in a vacuum oven overnight. All electrochemical measurements were carried

out by using CR 2032 coin-type cells (provided by DLG battery Co., Ltd, Shanghai, China). The coin-type cells were assembled in an Ar-filled glove box (Mbraun, Unilab, Germany) by stacking a porous polypropylene separator containing liquid electrolyte between the MoO<sub>3</sub>/graphene film electrodes and the lithium foil counter electrode. The electrolyte used was 1 M LiPF<sub>6</sub> in a 50:50 (v/v) mixture of ethylene carbonate (EC) and dimethyl carbonate (DMC), provided by MERCK KgaA, Germany. Charge–discharge tests were carried out by using a battery testing device (Land Battery Tester) interfaced to a computer with software. The system is capable of switching between charge and discharge automatically, according to the pre-set cut-off potentials. The cells were cycled between 1.5 and 3.5 V with a constant current of 100 mA g<sup>−1</sup>. Cyclic voltammetry (CV) was performed using a VMP3 Biologic electrochemistry workstation at a scan rate of 0.1 mV s<sup>−1</sup>.

### 3. Results and discussion

MoO<sub>3</sub> nanobelts are synthesized by microwave hydrothermal treatment using hydrogen peroxide, which is found to be a rapid and facile method for the preparation of MoO<sub>3</sub> nanobelts. The X-ray diffraction (XRD) patterns of the samples are presented in Fig. 1(a). All the diffraction peaks can be indexed as orthorhombic MoO<sub>3</sub> phase with the lattice parameters  $a = 3.96$  Å,  $b = 13.86$  Å, and

$c = 3.70$  Å, in good agreement with the literature values (JCPDS card no. 35–0609). No characteristic peaks of impurities were detected in these patterns. The strong intensity of the (0 2 0), (0 4 0), and (0 6 0) diffraction peaks of the MoO<sub>3</sub> nanobelts indicate that there is a preferred orientation of the MoO<sub>3</sub> nanobelts [21,46]. The peak intensity of the pristine MoO<sub>3</sub> nanobelts is obviously stronger than that of the diffraction peaks for the powder samples. This can be mainly attributed to the morphology of the nanobelts, which is characterized by a strong crystallinity. The XRD patterns of the MoO<sub>3</sub>/graphene hybrids show no evidence of diffraction peaks resulting from graphite oxide, indicating that the graphite oxide is reduced to graphene upon hydrothermal treatment. Due to the strong intensities of the diffraction peaks from the crystalline MoO<sub>3</sub> nanobelts, however, the characteristic broad diffraction peak with low intensity around 26°, corresponding to graphene, is not observed in the XRD pattern of the MoO<sub>3</sub>/graphene composite.

Raman spectra of graphene, MoO<sub>3</sub>, and MoO<sub>3</sub>/graphene film are shown in Fig. 1(b). Two characteristic bands are observed in the Raman spectrum of graphene: the one centred at 1324 cm<sup>−1</sup> (D band) is attributed to local defects/disorder, and the other at 1585 cm<sup>−1</sup> (G band) can be assigned to the sp<sup>2</sup> graphitized structure [47], while the Raman spectrum of the MoO<sub>3</sub>/graphene film reveals that the D and G bands appear at about 1328 and 1592 cm<sup>−1</sup>, respectively. The Raman spectrum of the MoO<sub>3</sub>/graphene film also

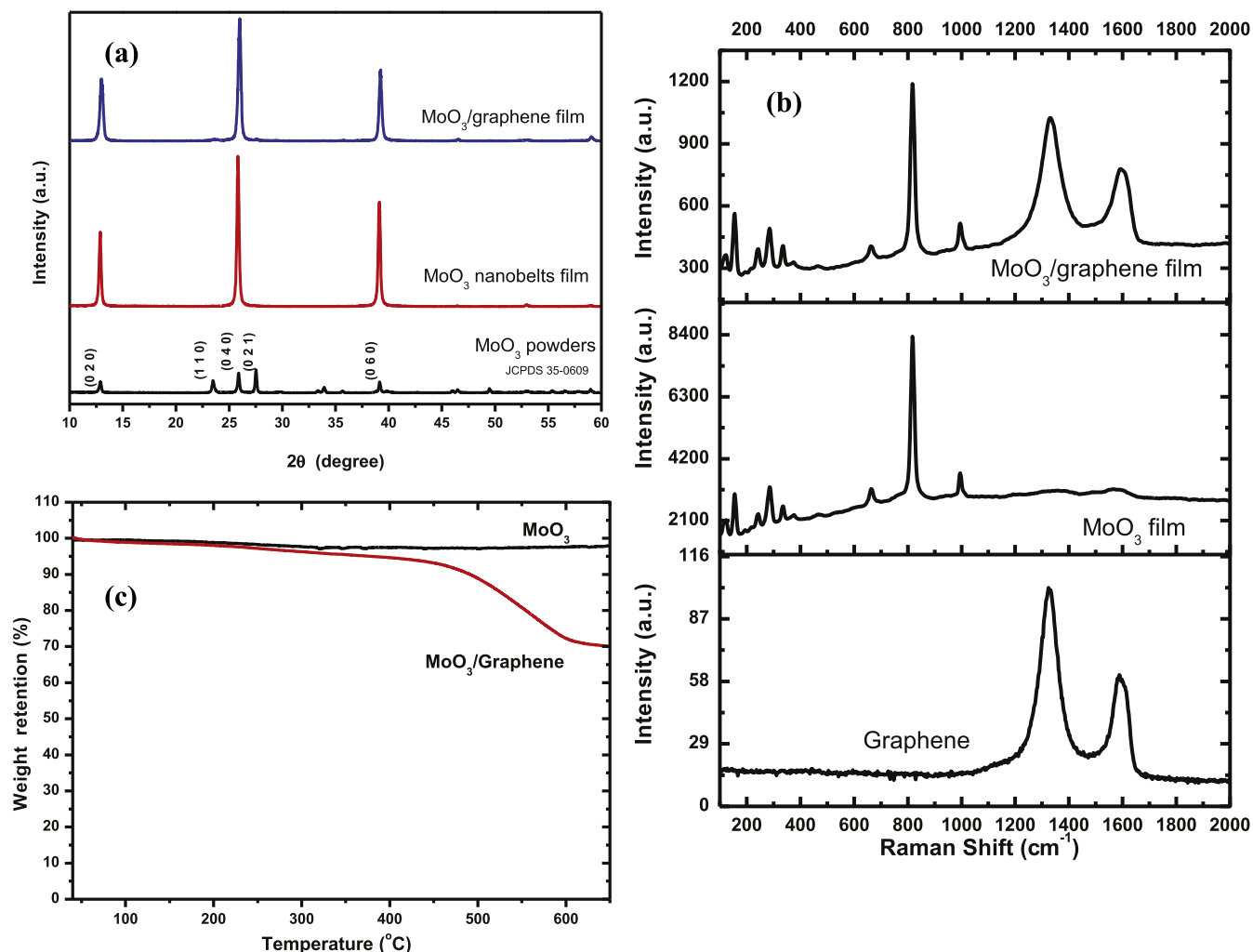


Fig. 1. (a) XRD patterns of MoO<sub>3</sub> film, MoO<sub>3</sub>/graphene film, and commercial MoO<sub>3</sub> powders; (b) Raman spectra of MoO<sub>3</sub>/graphene film, MoO<sub>3</sub>, and graphene; (c) TGA curves of MoO<sub>3</sub> and MoO<sub>3</sub>/graphene film.

shows three sharp characteristic bands of  $\text{MoO}_3$ . The Raman bands at  $995\text{ cm}^{-1}$  and  $817\text{ cm}^{-1}$  can be assigned to the asymmetrical and symmetrical stretching vibrations of the terminal  $\text{Mo}=\text{O}$  bonds, while the band at  $664\text{ cm}^{-1}$  is attributed to the asymmetrical stretching vibration of  $\text{O}-\text{Mo}-\text{O}$  bonds [48]. Peaks observed in the range of  $100\text{--}400\text{ cm}^{-1}$  correspond to various bending modes of  $\alpha\text{-MoO}_3$  crystal.

For quantifying the amount of graphene in the  $\text{MoO}_3$ /graphene composite material, TGA is carried out in air (Fig. 1(c)). The samples are heated from  $30$  to  $650^\circ\text{C}$  at a rate of  $10^\circ\text{C min}^{-1}$ . No obvious mass loss is observed up to  $650^\circ\text{C}$  for the as-prepared  $\text{MoO}_3$ , indicating that the bare  $\text{MoO}_3$  remains stable over the entire temperature range. As the  $\text{MoO}_3$  remains stable over this temperature range, any weight change is believed to correspond to the oxidation of graphene [49]. Therefore, the change in weight before and after the oxidation of graphene directly translates into the amount of graphene in the  $\text{MoO}_3$ /graphene film. By the use of this method, it is estimated that the amount of graphene is approximately 30 wt.%.

Field emission SEM (FESEM) observations of the  $\text{MoO}_3$  nanobelts and the  $\text{MoO}_3$ /graphene film are presented in Fig. 2. The FESEM secondary electron image of the pristine  $\text{MoO}_3$  nanobelt film (Fig. 2(a)) shows uniformly straight nanobelts  $\sim 200\text{--}800\text{ nm}$  in width and several micrometers in length. A side view of the  $\text{MoO}_3$  film (Fig. 2(b)) indicates that the  $\text{MoO}_3$  film is composed of very densely packed layers, so that the thickness of the flexible electrode is around  $50\text{ }\mu\text{m}$ . On the other hand, the  $\text{MoO}_3$ /graphene film (Fig. 2(c)) shows a similar morphology to that of the  $\text{MoO}_3$ , with the nanobelts lying on the stacked graphene sheets. Photographs of as-prepared free-standing  $\text{MoO}_3$ /graphene films peeled

off from PVDF membranes are shown in Fig. 2(d). The  $\text{MoO}_3$ /graphene paper is flexible, so that it can be bent to any curvature without breaking off and then returned to its original shape, while still maintaining its useful properties.

TEM and HRTEM (Fig. 3) reveal further information about the morphology and structure of the  $\text{MoO}_3$ /graphene films. Morphologies comprise either individual belts (Fig. 3(a)) or groups of thin belts lying on layers of graphene, as indicated in Fig. 3(b) and the associated high magnification inset. Bright field imaging combined with selected area electron diffraction investigations (Fig. 3(c)) indicates that the  $\text{MoO}_3$  growth direction is parallel to  $[001]$ . In this figure the zone axis is almost parallel to  $[010]$   $\text{MoO}_3$ . High-resolution imaging (Fig. 3(d)) of the area indicated in Fig. 3(c) also confirms the growth direction and reveals a deformed  $\text{MoO}_3$  lattice, structure typical of thin sheet materials and similar to that reveals in other HRTEM investigations of  $\text{MoO}_3$  nanobelts [50].

The electrochemical behaviour of  $\text{MoO}_3$  the nanobelts and  $\text{MoO}_3$ /graphene film is characterized by cyclic voltammetry (CV) at the scanning rate of  $0.1\text{ mV s}^{-1}$  between  $1.5$  and  $3.5\text{ V}$ , as shown in Fig. 4. The cathodic peaks located around  $2.6$  and  $2.17\text{ V}$  are obtained from both samples during the negative scan from  $3.5$  to  $1.5\text{ V}$ . These two reduction peaks correspond to two consecutive  $\text{Li}^+$  intercalations into the film electrode. It is reported that the lithium ions can insert themselves not only into the interlayer spacing between the  $[\text{MoO}_6]$  octahedron layers but also into the  $[\text{MoO}_6]$  octahedron intralayers [51]. The cathodic peak at  $2.6\text{ V}$  can be assigned to the irreversible lithium insertion into the crystal structure (probably into the  $[\text{MoO}_6]$  intralayers), which tends to trigger unrecoverable structural transformation of  $\text{MoO}_3$  [51,52]. The anodic peak located at  $2.53\text{ V}$  for both the  $\text{MoO}_3$  film and the

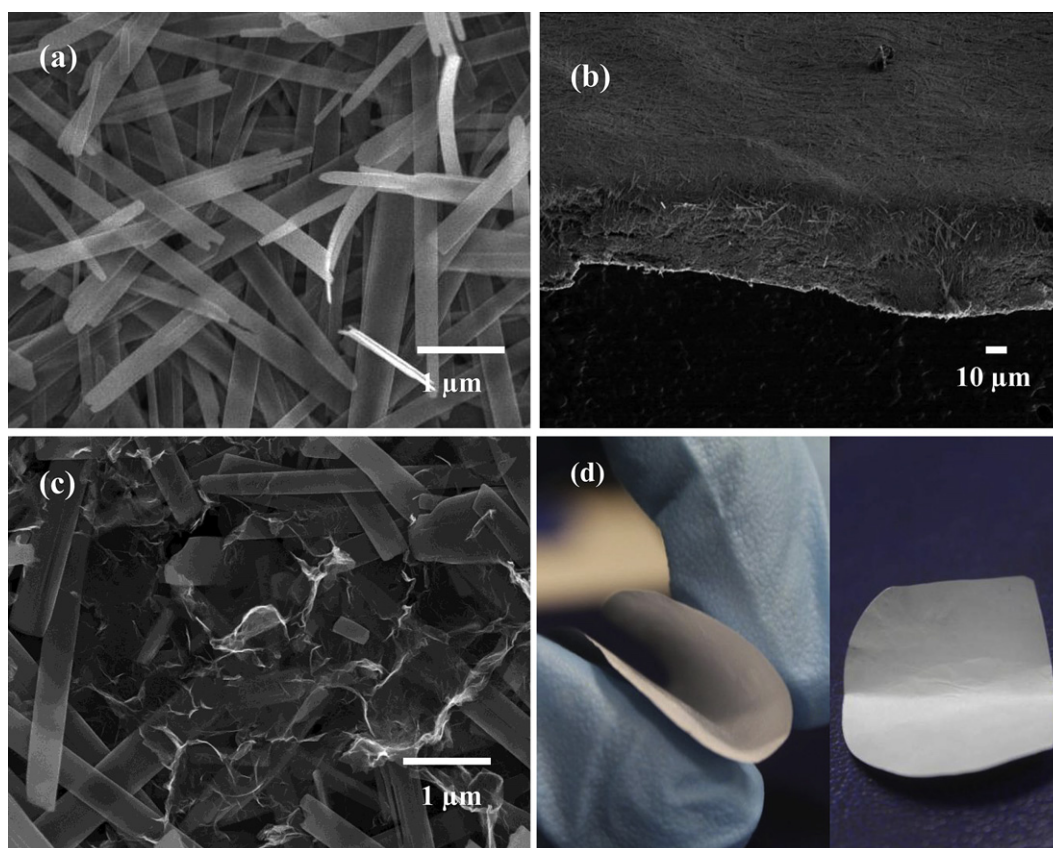


**Fig. 2.** FESEM secondary electron and optical images: (a) top view of free-standing  $\text{MoO}_3$  film, (b) And cross-sectional view at low magnification of free-standing  $\text{MoO}_3$  film; (c)  $\text{MoO}_3$ /graphene film, and (d) Photographs demonstrating the flexibility of the  $\text{MoO}_3$ /graphene film.



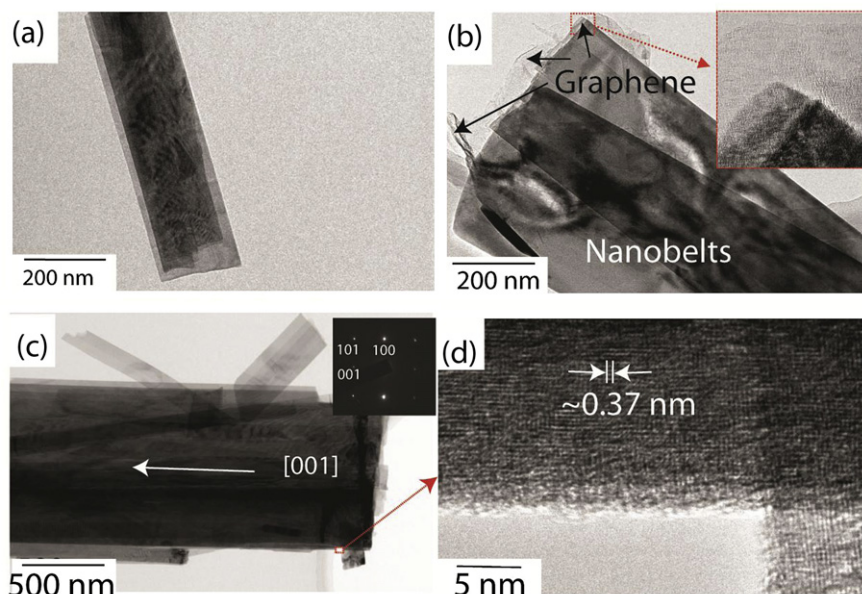


**Fig. 3.** TEM and HRTEM images of MoO<sub>3</sub>/graphene film: (a) low magnification image of a single nanobelt, (b) MoO<sub>3</sub> nanobelts coated with graphene, as indicated by arrows and higher magnification inset image, (c) Bright field image of nanobelt and associated electron diffraction pattern (near [010] zone axis) indicating an [001] growth direction, and (d), HRTEM image of indicated region in (c) with 0.37 nm spacing consistent with (001)MoO<sub>3</sub>.

MoO<sub>3</sub>/graphene film during the positive scan from 1.5 to 3.5 V corresponds to the reversible insertion of lithium ions into the interlayer spacings (van der Waals spacings) between the [MoO<sub>6</sub>] octahedron layers [51]. The first anodic and cathodic peaks of the MoO<sub>3</sub> film are broader, while the MoO<sub>3</sub>/graphene film exhibits sharper, more intense peaks. This strong hint indicates the good electrode kinetics of the MoO<sub>3</sub>/graphene electrode.

The initial charge–discharge profiles for the MoO<sub>3</sub> and MoO<sub>3</sub>/graphene composite electrodes at charge/discharge rates from 100 to 2000 mA g<sup>−1</sup> are shown in Fig. 5(a, b). For the MoO<sub>3</sub> and MoO<sub>3</sub>/graphene samples, the discharge and the charge curves have two voltage plateaus due to Li<sup>+</sup> intercalation into the film electrode, which is consistent with the material prepared by hydrothermal treatment of a peroxomolybdic acid solution [21]. This also agrees with the results on cathodic and anodic peak potential in the cyclic voltammograms. Initial discharge capacities are measured to be 307 and 291 mAh g<sup>−1</sup> at 100 mA g<sup>−1</sup>, and 123 and 151 mAh g<sup>−1</sup> at

2000 mA g<sup>−1</sup> for the MoO<sub>3</sub> and MoO<sub>3</sub>/graphene film electrodes, respectively. The discharge capacity decreases for all samples with increasing current density, and for the MoO<sub>3</sub> sample, the difference between the two plateaus becomes larger. The MoO<sub>3</sub> sample delivers sloping charge/discharge curves instead of a flat plateau (Fig. 5(a)) compared to the MoO<sub>3</sub>/graphene sample, which still maintains a flat plateau in its charge/discharge curves even at the current density of 1000 mA g<sup>−1</sup>. In addition, the MoO<sub>3</sub>/graphene sample shows that the separation between the redox couple is small, and the CV curves for the second and third cycles generally overlap, suggesting the good reversibility of lithium ion insertion/extraction in the van der Waals spacings of the MoO<sub>3</sub>/graphene sample.

The cycling performance of the MoO<sub>3</sub>/graphene at 100 mA g<sup>−1</sup> with that of the MoO<sub>3</sub> in the voltage range of 1.5–3.5 V is demonstrated in Fig. 5(c). The MoO<sub>3</sub>/graphene electrode shows a higher capacity and better cycling performance. After 100 cycles, the discharge capacity for the MoO<sub>3</sub>/graphene electrode is

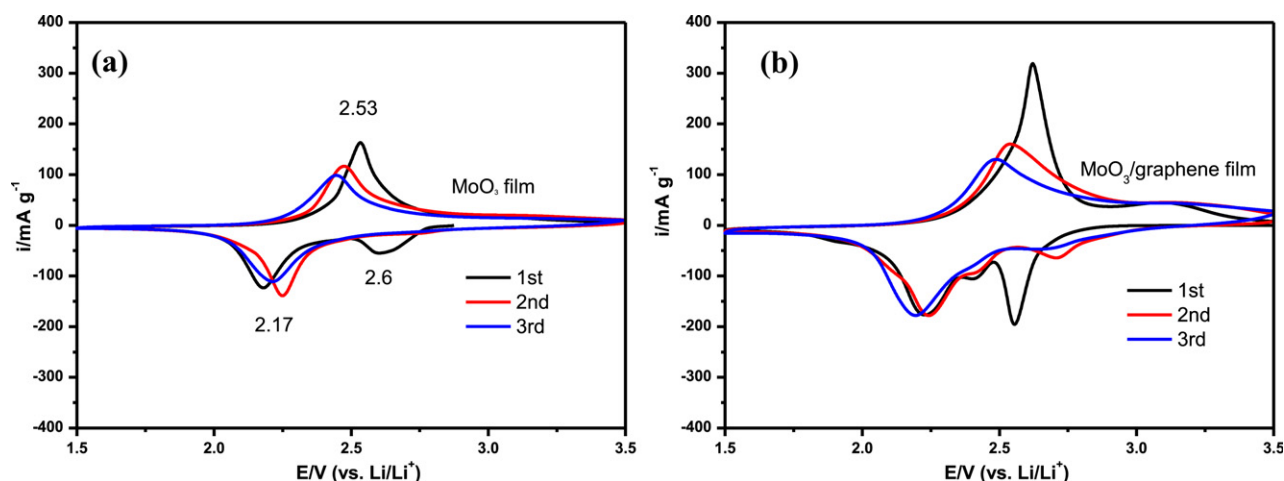


**Fig. 4.** Typical CV profiles for the first 3 cycles of MoO<sub>3</sub> film (a) and MoO<sub>3</sub>/graphene film (b) at scan rate of 0.1 mV s<sup>−1</sup>.

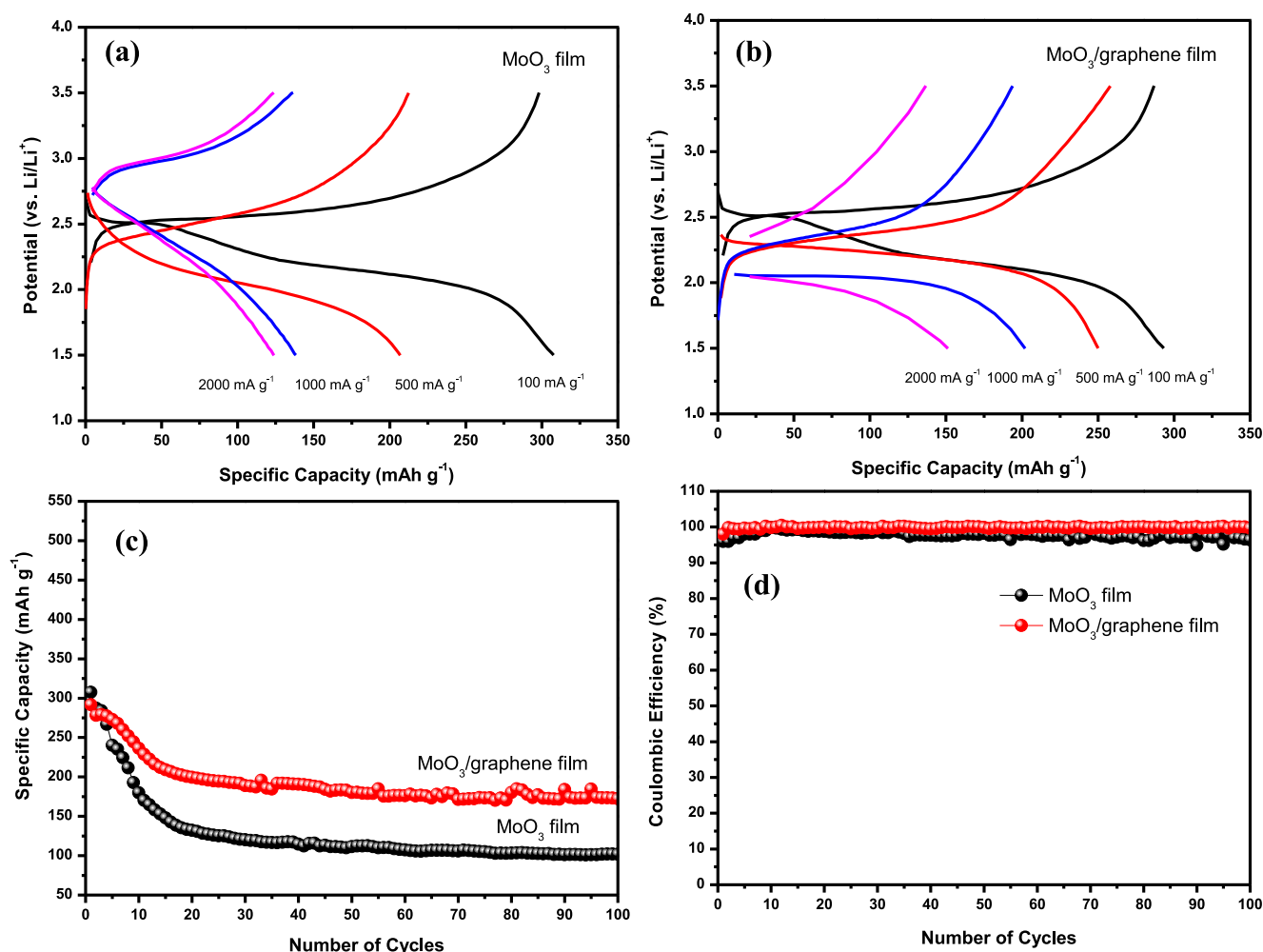


**Fig. 5.** The initial galvanostatic charge–discharge profile of (a) MoO<sub>3</sub> film electrode, (b) MoO<sub>3</sub>/graphene film electrode at different current densities from 100 to 2000 mA g<sup>-1</sup> between 1.5 and 3.5 V; (c) Cycling performance beyond 100 cycles at 100 mA g<sup>-1</sup>; (d) Coulombic efficiency.

measured to be 172 mAh g<sup>-1</sup> at 100 mA g<sup>-1</sup> (59% of initial discharge capacity), with an initial coulombic efficiency of 98% (Fig. 5(d)). On the contrary, the discharge capacity for the MoO<sub>3</sub> electrode was only 101 mAh g<sup>-1</sup> (32% of initial discharge capacity) at 100 mA g<sup>-1</sup>, with an initial coulombic efficiency of 96%. The high capacity and good cycling performance delivered by the MoO<sub>3</sub>/graphene electrode can be attributed to the graphene in the MoO<sub>3</sub>/graphene film electrode, which evidently aids the Li<sup>+</sup> intercalation into the Li<sub>x</sub>-MoO<sub>3</sub> lattice of the MoO<sub>3</sub>/graphene electrode, by improving both the accessibility for Li<sup>+</sup> ions and the electrical conductivity [26]. Graphene in the MoO<sub>3</sub>/graphene film electrode can connect the isolated MoO<sub>3</sub> nanobelts and gives rise to valid conductive networks in the electrodes.

Electrochemical impedance spectroscopy (EIS) measurements are carried out in order to compare the conductivity of the prepared MoO<sub>3</sub> and MoO<sub>3</sub>/graphene electrodes. To achieve stable solid electrolyte interphase (SEI) formation and the percolation of electrolyte through the electrode materials, the impedance measurements are performed after running charge–discharge for 5 cycles at a discharge potential of 2.5 V vs. Li/Li<sup>+</sup>. The Nyquist plots of the two electrodes, as well as the fitting results using an equivalent circuit are depicted in Fig. 6(a). In this equivalent circuit (inset),  $R_{\Omega}$  and  $R_{ct}$  are the ohmic resistance (total resistance of the electrolyte, separator, and electrical contacts) and charge-transfer resistance, respectively. CPE is the constant phase-angle element, involving

double layer capacitance, and  $W$  represents the Warburg impedance, reflecting the solid-state diffusion of Li ions into the bulk of the active materials, which is associated with the inclined line at low frequencies [53]. It can be seen clearly that the  $R_{ct}$  is much smaller for the MoO<sub>3</sub>/graphene ( $R_{ct} = 216.5 \Omega$ ) electrode than for the MoO<sub>3</sub> ( $R_{ct} = 640.8 \Omega$ ) electrode after the 5th cycle, which indicates that the graphene coating could enable much easier charge transfer at the electrode/electrolyte interface and consequently, decrease the overall battery internal resistance. The graphene coating applied in the synthesis significantly enhances the conductivity of the MoO<sub>3</sub>/graphene material, since the conductive graphene facilitates electronic conductive paths in the MoO<sub>3</sub> nanobelts, which is considered a key factor in improving the discharge capacity, rate capability, and cycle life of the MoO<sub>3</sub>/graphene material. Besides the increased conductivity of the electrode due to graphene during charge and discharge cycling, the high performance of the MoO<sub>3</sub>/graphene film is strongly related to the nanobelt morphology of the MoO<sub>3</sub> cathode material. MoO<sub>3</sub> nanobelts have a large surface area, which will reduce the actual effective current density on the active material and relieve the strain induced by the volume change during the electrochemical reaction. Moreover, due to the flexibility of the MoO<sub>3</sub> nanobelts, the morphology of the MoO<sub>3</sub> nanobelts can be preserved during the Li<sup>+</sup> insertion/extraction process, even after 100 cycles, as shown in Fig. 6(b).

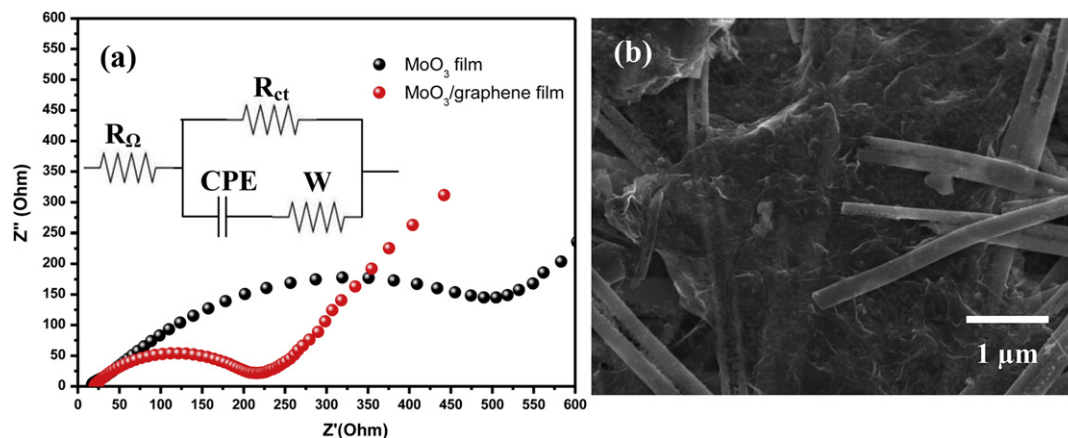


Fig. 6. Nyquist plots for the MoO<sub>3</sub>/graphene film electrode after running charge–discharge for 5 cycles at a discharge potential of 2.5 V vs. Li/Li<sup>+</sup> and fitting results using the equivalent circuit shown in the inset (a), and FESEM image of MoO<sub>3</sub>/graphene film electrode after charge–discharge for 100 cycles (b).

#### 4. Conclusions

In this work, free-standing flexible MoO<sub>3</sub>/graphene film electrode is prepared by a two-step, ultra-fast, microwave hydrothermal method and then followed by vacuum filtration technique. The hybrid material, consisting of a layer-structured metal oxide, MoO<sub>3</sub>, and graphene results in a synergistic interaction between the inorganic and organic components. The charge–discharge measurements show that the MoO<sub>3</sub>/graphene film delivers a significantly higher reversible capacity and excellent cycling stability (172 mAh g<sup>−1</sup> at 100 mA g<sup>−1</sup> after 100 cycles) compared to the pristine MoO<sub>3</sub> film. The results show that the MoO<sub>3</sub>/graphene designed in this study can be used as a flexible cathode material for rechargeable bendable Li-ion batteries. The MoO<sub>3</sub>/graphene film electrodes have higher specific capacities than the MoO<sub>3</sub> film electrode, since the conductive graphene facilitates electronic conductive paths in the MoO<sub>3</sub> nanobelts, and the good performance is also related to the nanobelt morphology of the MoO<sub>3</sub> cathode material.

#### Acknowledgements

Financial support provided by the Australian Research Council (ARC) through the ARC Centre of Excellence for Electromaterials Science and a Discovery Project (DP0987805) are gratefully acknowledged. The authors acknowledge use of facilities within the UOW Electron Microscopy Centre. Many thanks also go to Dr. T. Silver for critical reading of the manuscript.

#### References

- [1] D. Liu, G. Cao, *Energy Environ. Sci.* 3 (2010) 1218–1237.
- [2] H. Nishide, K. Oyaizu, *Science* 319 (2008) 737–738.
- [3] L. Hu, H. Wu, F. La Mantia, Y. Yang, Y. Cui, *ACS Nano* 4 (2010) 5843–5848.
- [4] K.T. Nam, D.-W. Kim, P.J. Yoo, C.-Y. Chiang, N. Meethong, P.T. Hammond, Y.-M. Chiang, A.M. Belcher, *Science* 312 (2006) 885–888.
- [5] E. Hosono, T. Kudo, I. Honma, H. Matsuda, H. Zhou, *Nano Lett.* 9 (2009) 1045–1051.
- [6] D.K. Kim, P. Muralidharan, H.-W. Lee, R. Ruffo, Y. Yang, C.K. Chan, H. Peng, R.A. Huggins, Y. Cui, *Nano Lett.* 8 (2008) 3948–3952.
- [7] Y. Yang, C. Xie, R. Ruffo, H. Peng, D.K. Kim, Y. Cui, *Nano Lett.* 9 (2009) 4109–4114.
- [8] C.K. Chan, H. Peng, R.D. Twisten, K. Jarausch, X.F. Zhang, Y. Cui, *Nano Lett.* 7 (2007) 490–495.
- [9] S.-L. Chou, J.-Z. Wang, J.-Z. Sun, D. Wexler, M. Forsyth, H.-K. Liu, D.R. MacFarlane, S.-X. Dou, *Chem. Mater.* 20 (2008) 7044–7051.
- [10] J.-Z. Wang, S.-L. Chou, H. Liu, G.X. Wang, C. Zhong, S. Yen Chew, H. Kun Liu, *Mater. Lett.* 63 (2009) 2352–2354.
- [11] K.H. Seng, J. Liu, Z.P. Guo, Z.X. Chen, D. Jia, H.K. Liu, *Electrochem. Comm.* 13 (2011) 383–386.
- [12] L.Q. Mai, B. Hu, W. Chen, Y.Y. Qi, C.S. Lao, R.S. Yang, Y. Dai, Z.L. Wang, *Adv. Mater.* 19 (2007) 3712–3716.
- [13] S.-H. Lee, Y.-H. Kim, R. Deshpande, P.A. Parilla, E. Whitney, D.T. Gillaspie, K.M. Jones, A.H. Mahan, S. Zhang, A.C. Dillon, *Adv. Mater.* 20 (2008) 3627–3632.
- [14] N.A. Chernova, M. Roppolo, A.C. Dillon, M.S. Whittingham, *J. Mater. Chem.* 19 (2009) 2526–2552.
- [15] L. Zheng, Y. Xu, D. Jin, Y. Xie, *J. Mater. Chem.* 20 (2010) 7135–7143.
- [16] T. Brezesinski, J. Wang, S.H. Tolbert, B. Dunn, *Nat. Mater.* 9 (2010) 146–151.
- [17] E. Comini, L. Yubao, Y. Brando, G. Sberveglieri, *Chem. Phys. Lett.* 407 (2005) 368–371.
- [18] M. Sadakane, N. Watanabe, T. Katou, Y. Nodasaka, W. Ueda, *Angew. Chem. Int. Edition* 46 (2007) 1493–1496.
- [19] H. Tsuji, Y. Koyasu, *J. Am. Chem. Soc.* 124 (2002) 5608–5609.
- [20] X.W. Lou, H.C. Zeng, *Chem. Mater.* 14 (2002) 4781–4789.
- [21] L. Zhou, L. Yang, P. Yuan, J. Zou, Y. Wu, C. Yu, *J. Phys. Chem. C* 114 (2010) 21868–21872.
- [22] T. Tao, A.M. Glushenkov, C. Zhang, H. Zhang, D. Zhou, Z. Guo, H.K. Liu, Q. Chen, H. Hu, Y. Chen, *J. Mater. Chem.* 21 (2011) 9350–9355.
- [23] M.M. Rahman, J.-Z. Wang, N.H. Idris, Z. Chen, H. Liu, *Electrochim. Acta* 56 (2010) 693–699.
- [24] H. Gwon, H.-S. Kim, K.U. Lee, D.-H. Seo, Y.C. Park, Y.-S. Lee, B.T. Ahn, K. Kang, *Energy Environ. Sci.* 4 (2011) 1277–1283.
- [25] L. Cui, J. Li, X.-g. Zhang, *Mater. Lett.* 63 (2009) 683–686.
- [26] Y. Kim, J.-S. Kim, M.-T. Thieu, H.-C. Dinh, I.-H. Yeo, W.I. Cho, S.-i. Mho, *Bull. Korean Chem. Soc.* 31 (2010) 3109.
- [27] S. Park, R.S. Ruoff, *Nat. Nanotech.* 4 (2009) 217–224.
- [28] J. Liang, Y. Xu, D. Sui, L. Zhang, Y. Huang, Y. Ma, F. Li, Y. Chen, *J. Phys. Chem. C* 114 (2010) 17465–17471.
- [29] G. Zhou, D.-W. Wang, F. Li, L. Zhang, N. Li, Z.-S. Wu, L. Wen, G.Q. Lu, H.-M. Cheng, *Chem. Mater.* 22 (2010) 5306–5313.
- [30] J.-Z. Wang, C. Zhong, D. Wexler, N.H. Idris, Z.-X. Wang, L.-Q. Chen, H.-K. Liu, *Chem. Eur. J.* 17 (2011) 661–667.
- [31] I.R.M. Kottogoda, N.H. Idris, L. Lu, J.-Z. Wang, H.-K. Liu, *Electrochim. Acta* 56 (2011) 5815–5822.
- [32] Y.J. Mai, S.J. Shi, D. Zhang, Y. Lu, C.D. Gu, J.P. Tu, *J. Power Sources* 204 (2012) 155–161.
- [33] X. Wang, X. Zhou, K. Yao, J. Zhang, Z. Liu, *Carbon* 49 (2011) 133–139.
- [34] C. Zhu, Y. Fang, D. Wen, S. Dong, *J. Mater. Chem.* 21 (2011) 16911–16917.
- [35] C. Zhong, J. Wang, Z. Chen, H. Liu, *J. Phys. Chem. C* 115 (2011) 25115–25120.
- [36] Y. Shi, S.-L. Chou, J.-Z. Wang, D. Wexler, H.-J. Li, H.-K. Liu, Y. Wu, *J. Mater. Chem.* 22 (2012) 16465–16470.
- [37] X. Zhou, F. Wang, Y. Zhu, Z. Liu, *J. Mater. Chem.* 21 (2011) 3353–3358.
- [38] R.-Q. Song, A.-W. Xu, B. Deng, Y.-P. Fang, *J. Phys. Chem. B* 109 (2005) 22758–22766.
- [39] L. Zheng, Y. Xu, D. Jin, Y. Xie, *Chem. Mater.* 21 (2009) 5681–5690.
- [40] T. Xia, Q. Li, X. Liu, J. Meng, X. Cao, *J. Phys. Chem. B* 110 (2006) 2006–2012.
- [41] P. Zhang, S. Yin, T. Sato, *Appl. Catal. B Environ.* 89 (2009) 118–122.
- [42] J.-H. Lee, C.-K. Kim, S. Katoh, R. Murakami, *J. Alloys Compounds* 325 (2001) 276–280.
- [43] A. Phururangrat, D.J. Ham, S. Thongtem, J.S. Lee, *Electrochem. Commun.* 11 (2009) 1740–1743.
- [44] D.C. Marcano, D.V. Kosynkin, J.M. Berlin, A. Sinitskii, Z. Sun, A. Slesarev, L.B. Alemany, W. Lu, J.M. Tour, *ACS Nano* 4 (2010) 4806–4814.
- [45] W.A. De Heer, W.S. Bacs, A. Chatelain, T. Gerfin, R. Humphrey-Baker, L. Forro, D. Ugarte, *Science* 268 (1995) 845–847.
- [46] C.V. Subba Reddy, Z.R. Deng, Q.Y. Zhu, Y. Dai, J. Zhou, W. Chen, S.I. Mho, *Appl. Phys. A: Mater. Sci. Process.* 89 (2007) 995–999.

- [47] A.C. Ferrari, J. Robertson, *Phys. Rev. B* 61 (2000) 14095–14107.
- [48] X. Yang, H. Ding, D. Zhang, X. Yan, C. Lu, J. Qin, R. Zhang, H. Tang, H. Song, *Crystal Res. Tech.* 46 (2011) 1195–1201.
- [49] S. Park, J. An, J.R. Potts, A. Velamakanni, S. Murali, R.S. Ruoff, *Carbon* 49 (2011) 3019–3023.
- [50] Y.L. Xie, F.C. Cheong, Y.W. Zhu, B. Varghese, R. Tamang, A.A. Bettiol, C.H. Sow, *J. Phys. Chem. C* 114 (2009) 120–124.
- [51] W. Li, F. Cheng, Z. Tao, J. Chen, *J. Phys. Chem. B* 110 (2005) 119–124.
- [52] J.S. Chen, Y.L. Cheah, S. Madhavi, X.W. Lou, *J. Phys. Chem. C* 114 (2010) 8675–8678.
- [53] G.T.-K. Fey, C.-Z. Lu, T.P. Kumar, *J. Power Sources* 115 (2003) 332–345.